

Vibrational spectroscopy analysis of ligand efficacy in M2R

Kota Katayama (✉ katayama.kota@nitech.ac.jp)

Nagoya Institute of Technology

Kohei Suzuki

Nagoya Institute of Technology

Ryoji Suno

Kansai Medical University

Ryoji Kise

Tohoku University

Hirokazu Tsujimoto

Kyoto University

So Iwata

Kyoto University

Asuka Inoue

Tohoku University

Takuya Kobayashi

Kansai Medical University

Hideki Kandori

Nagoya Institute of Technology <https://orcid.org/0000-0002-4922-1344>

Article

Keywords: G protein-coupled receptors (GPCRs), ligand binding, human M2 muscarinic acetylcholine receptor (M2R)

Posted Date: April 16th, 2021

DOI: <https://doi.org/10.21203/rs.3.rs-411771/v1>

License:  This work is licensed under a Creative Commons Attribution 4.0 International License.

[Read Full License](#)

Version of Record: A version of this preprint was published at Communications Biology on November 23rd, 2021. See the published version at <https://doi.org/10.1038/s42003-021-02836-1>.

1 **Vibrational spectroscopy analysis of ligand efficacy in M₂R**

2 Kota Katayama*^{1,2,3,8}, Kohei Suzuki^{1,8}, Ryoji Suno⁴, Ryoji Kise⁵, Hirokazu Tsujimoto⁶, So Iwata⁶,
3 Asuka Inoue⁵, Takuya Kobayashi^{4,7}, and Hideki Kandori*^{1,2}

4

5 ¹Department of Life Science and Applied Chemistry, Nagoya Institute of Technology, Showa-ku,
6 Nagoya 466-8555, Japan

7 ²OptoBioTechnology Research Center, Nagoya Institute of Technology, Showa-ku, Nagoya
8 466-8555, Japan

9 ³PRESTO, Japan Science and Technology Agency, 4-1-8 Honcho, Kawaguchi, Saitama 332-0012,
10 Japan

11 ⁴Department of Medical Chemistry, Kansai Medical University, Hirakata 573-1010, Japan

12 ⁵Graduate School of Pharmaceutical Sciences, Tohoku University, Sendai, Miyagi 980-8578,
13 Japan

14 ⁶Department of Cell Biology and Medical Chemistry, Graduate School of Medicine, Kyoto
15 University, Kyoto 606-8501, Japan

16 ⁷Japan Agency for Medical Research and Development, Core Research for Evolutional Science
17 and Technology (AMED-CREST), Chiyoda-ku, Tokyo 100-0004, Japan

18 ⁸These authors contributed equally

19

20 *Correspondence and requests for materials should be addressed to K.K. (email:
21 Katayama.kota@nitech.ac.jp), H.K. (email: kandori@nitech.ac.jp)

22

23 **Abstract**

24 The intrinsic efficacy of ligand binding to G protein-coupled receptors (GPCRs) reflects the
25 ability of the ligand to differentially activate its receptor to cause a physiological effect. Here we
26 use attenuated total reflection-Fourier transform infrared (ATR-FTIR) spectroscopy to examine
27 the ligand-dependent conformational changes in the human M₂ muscarinic acetylcholine receptor
28 (M₂R). We show that different ligands affect conformational alteration appearing at the C=O
29 stretch of amide-I band in M₂R. Notably, ATR-FTIR signals strongly correlated with G-protein
30 activation levels in cells. Together, we propose that amide-I band serves as an infrared probe to
31 distinguish the ligand efficacy in M₂R and paves the path to rationally design ligands with varied
32 efficacy towards the target GPCR.

33

34 **Introduction**

35 G protein-coupled receptors (GPCRs) are one of the largest family of membrane proteins that
36 induce most of the intracellular biological signalling upon ligand binding¹. Therefore,
37 understanding the molecular mechanism of GPCR-ligand interaction is vital to elucidating their
38 physiological functions and pathologies. GPCR signalling utilizes a coupling mechanism between
39 the extracellular facing ligand-binding pocket and the cytoplasmic domain of the receptor that
40 selectively interacts with the signalling transducer such as G-proteins, β -arrestins and various
41 other effectors^{2,3}. Furthermore, the different levels of activation of GPCRs are selectively and
42 specifically controlled by the type of ligand, commonly known as efficacy⁴⁻⁶. To date, ligands
43 have been categorized into four groups: full agonists, partial agonists, neutral antagonists, and
44 inverse agonists. Understanding the molecular mechanisms that determine the ligand efficacy of
45 GPCRs is important for rational drug design. In addition, discovery of ligands that regulate a
46 target activity has contributed largely to the understanding of both physiological and pathological
47 processes. However, most methods of evaluating ligand efficacy use downstream biochemical

48 and physiological responses that measures the second messenger productivity, protein
49 phosphorylation, and the level of gene expression⁷⁻⁹, and therefore these methods cannot evaluate
50 the ligand efficacy directly.

51 Over the last decade, a number of high-resolution X-ray crystal structures of GPCRs have
52 been determined by using lipid cubic phase (LCP). In addition, recent advance of single particle
53 analyses using cryo electron microscopy provided not only the inactive structures bound with
54 either antagonist or inverse agonist, but also active structures bound with agonists and signal
55 transducers¹⁰⁻¹³. These structures have elucidated key structural changes between the inactive and
56 the active conformations of GPCRs, especially in the extracellular ligand-binding site and the
57 cytoplasmic surface where the effector G-protein interacts¹⁰⁻¹³. The muscarinic acetylcholine
58 receptor 2 (M₂R), one of the most extensively studied GPCR has been crystallized with its
59 inverse agonist 3-quinuclidinyl-benzilate (QNB)¹⁴ or N-methylscopolamine (NMS)¹⁵, full agonist
60 Iperoxo (Ixo)¹⁶, and effector G_o-protein¹⁷. Although these studies have provided important
61 insights into the structural changes including the ligand pocket and TM6 movement mediated by
62 the two classes of ligands at the atomic level, its application to a broad variety of ligands with
63 different efficacies, especially partial agonists and neutral antagonists, is extremely challenging.
64 This is partly because most of the ligands have similar chemical and structural properties and
65 high their binding affinities ($K_i \leq 10$ nM) causes the GPCR receptors to adapt their low-energy
66 stable conformations. In addition, these structural techniques capture only a snapshot, low-energy
67 conformation, which lack the conformational heterogeneity, therefore these methods cannot fully
68 explain the mechanism of the efficacies.

69 Spectroscopic techniques such as nuclear magnetic resonance (NMR) and double
70 electron-electron resonance (DEER) have provided insights into the dynamic nature of GPCRs
71 underpinning the conformational plasticity of different efficacy ligand binding¹⁸⁻²³. However,
72 both spectroscopy techniques require large quantities of pure protein, isotopic labelling and/or

73 site-directed mutations, which might not be suitable for all membrane protein systems due to their
74 low labelling efficiency, expression limitations, misfolding, or loss of function. Attenuated total
75 reflection-Fourier transform infrared (ATR-FTIR) spectroscopy is a well-established
76 spectroscopy technique to study protein conformational changes related to their function, such as
77 enzymatic activation²⁴ or substrate or ligand recognition and binding²⁵. By combining a
78 two-liquid exchange system, perfusion-induced difference ATR-FTIR spectroscopy has been
79 applied to analyse ion-protein and ligand-protein interactions for ion channel and transporter
80 proteins, respectively²⁶⁻³¹. Another important advantage of this method is that ATR-FTIR
81 generally requires less than 5 µg of pure protein reconstituted into a lipid bilayer, which makes it
82 highly effective and economical to study GPCRs.

83 We have recently employed this technique on M₂R to reveal its ligand binding mechanism
84 with its natural agonist, acetylcholine (ACh) and its antagonist, atropine (Atro)³². While
85 ACh-bound spectra showed large spectral changes of the amide-I band (the C=O stretch of the
86 α-helix), Atro-bound spectra revealed an oppose spectral shift of amide-I, which indicates the
87 different conformational changes that occur between an agonist and an antagonist binding to M₂R.
88 Furthermore, by tracking the ligand concentration dependence on M₂R activity and ligand
89 binding/dissociation in real time, we could also measure physicochemical properties of ligand
90 binding with M₂R. Based on these results, we hypothesize that ATR-FTIR could be positioned as
91 a quick and economical structural analysis tool to examine the ligand binding with GPCRs.

92 To verify our hypothesis, here we perform systematic ligand binding-induced difference
93 ATR-FTIR spectroscopy measurements on ligands with different efficacies (inverse agonists to
94 full agonists). We observe distinct conformational changes among the agonists, partial agonists,
95 and antagonists in the C=O stretch of amide-I band, which correlates well with G-protein activity
96 in the cells. Time-course ATR-FTIR spectral traces at amide-I band demonstrate differential
97 kinetic patterns: fast dissociation for the full and partial agonists from M₂R and slow or no

98 dissociation for the antagonists and inverse agonists. Together, the amide-I band serves as an
99 infrared probe to distinguish the ligand efficacy of M₂R. Additionally, our analysis demonstrate
100 that chemically related ligands exhibit different efficacy.

101

102 **Results**

103 **Spectra of the agonists- and partial agonists-bound forms**

104 We selected four agonists that are structurally similar to ACh, including Metacholine (Meta),
105 Arecholine (Are), Carbamylcholine (Carb), Iperoxo (Ixo), and three partial agonists with no
106 structural similarity to ACh, including Pilocarpin (Pilo), McN-A-343 (McN), and Xanomeline
107 (Xano) (Fig. 1 a). All ligand binding-induced ATR-FTIR difference spectra contained combined
108 noise signals originating from the unbound ligand absorption, distortions from the buffer,
109 absorption changes in water, and the baseline drift due to protein shrinkage (Extended Data Fig.
110 1-5). After removing these distortions, the baseline-corrected spectra were calculated as shown in
111 Fig. 1b. The ATR-FTIR spectra of the agonist-bound forms were very similar in their spectral
112 features, except for Ixo. As we observed in ACh-bound M₂R spectra, all of the features including
113 three dominant bands 1666 (-)/1656 (+)/1640 (-) cm⁻¹ combination bands, positive 1687 cm⁻¹
114 band, and positive 1246 cm⁻¹ were detectable in Meta-, Are-, and Carb-bound spectra. A previous
115 study reported that the combination bands around 1650 cm⁻¹ are originated from C=O stretch of
116 amide-I band. Particularly, a 10 cm⁻¹ down-shift from 1666 to 1656 cm⁻¹ of amide-I band upon
117 binding of ACh points to an outward movement of TM6 enabling the engagement with G-protein.
118 Furthermore, two positive bands at 1687 and 1246 cm⁻¹ were tentatively assigned to C=O stretch
119 of Asn404^{6.52} (the numbers in parenthesis denote the residue position in the Ballesteros-Weinstein
120 scheme³³) and C-O stretch of tyrosine lid which is comprised of the three conserved tyrosines
121 (Tyr104^{3.33}, Tyr403^{6.51}, and Tyr426^{7.39}), respectively. Both, Asn404^{6.52} and the tyrosine lid
122 constitute the orthosteric ligand binding site of M₂R. Since these bands are conserved in Meta-,

123 Are-, and Carb-bound spectra, these agonists exhibit similar binding modes and associated
124 conformational changes in the M₂R protein moiety.

125 Unlike ACh- and other agonists-bound spectra, Ixo-bound spectra clearly showed a
126 distinctive spectral shift of amide-I band (Fig. 1b). Although the pair bands at 1666 (-)/1652
127 (-)/1631 (+) cm⁻¹ can be attributed to the C=O stretch of amide-I, they showed around 20-30 cm⁻¹
128 spectral downward shift as compared to other agonists-bound spectra. Ixo, being 100-fold more
129 potent than ACh and classified as a super agonist of M₂R³⁴, was used to obtain the active M₂R
130 crystal structure. Previously, solution NMR study in combination with molecular dynamics (MD)
131 simulations revealed significant protein conformational changes upon binding of full agonist and
132 super agonist with M₂R. Major conformational changes were found in TM5 and TM6, which
133 would be influenced by slight changes in the orthosteric-binding site of M₂R²². Namely, Ixo binds
134 deeper into the ligand binding pocket of M₂R than Ach via a hydrogen bond with Asn404^{6.52} and
135 a water molecule near Asn404^{6.52} 22. Interestingly, the Ixo-bound spectra shows a positive 1684
136 cm⁻¹ band which tentatively originates from the C=O stretch of Asn404^{6.52} with a 3 cm⁻¹
137 downward shift as compared to ACh-bound spectra (Fig. 1b). This suggests a stronger hydrogen
138 bond interaction of Ixo with Asn404^{6.52} than ACh. The observed changes in the hydrogen bond
139 strength particular to Ixo-binding is likely the reason of the distinct TM conformational change
140 detected as 20-30 cm⁻¹ downward shift of amide-I band.

141 In contrast to agonists, partial agonists-bound spectra display relatively different spectral
142 features. At around 1650 cm⁻¹ region, the band intensity and the population of the combination
143 band of amide-I (1666 (-)/1656 (+)/1640 (-) cm⁻¹ in ACh-bound spectra) were altered upon partial
144 agonists binding. However, the band frequencies were nearly identical to that of agonists-bound
145 spectra. In Pilo- and McN-bound spectra, while the bands at 1667 (-) or 1670 (-) cm⁻¹
146 corresponding to the apo form are decreased, negative 1643 or 1649 cm⁻¹ bands intensities were
147 enhanced. These pattern of spectral shift of amide-I bands are similar to that of Atro-bound

148 spectra (Fig. 1b). In contrast, Xano-bound spectra had 1666 (-)/1655 (+)/1643 (-) cm^{-1}
149 combination band intensity similar to that of agonists-bound spectra. The decrease in band
150 intensity of amide-I caused by partial agonists was consistent with their lower efficacy towards
151 M_2R . Thus, the spectral shift pattern of the amide-I band suggests that it is reflected in the
152 conformational equilibrium between the inactive state and active states of M_2R .

153 While similar protein structural changes were observed between agonists and partial
154 agonists which result in equilibrium shift from inactive to active states, partial agonists-dependent
155 conformational changes around ligand binding site were also observed. Similar to ACh-bound
156 spectra, Pilo-bound spectra shows two positive bands at 1687 and 1246 cm^{-1} , which originates
157 from Asn404^{6.52} and the tyrosine lid, respectively. Unlike Pilo-bound spectra, McN-bound spectra
158 does not show the positive band at 1687 cm^{-1} , and the positive band at 1246 cm^{-1} shifts to 1231
159 cm^{-1} . We also observed a 7 cm^{-1} up shift in Asn404^{6.52} signal to 1694 cm^{-1} and a 2 cm^{-1}
160 down-shift in tyrosine lid signal to 1244 cm^{-1} . These results suggest a different hydrogen bond
161 strength between the nitrogen of Asn404^{6.32} and the acetyl oxygen (in Pilo and McN) or sulphur
162 (in Xano) (Fig. 1a). This is one of the key reasons for the differential activation of M_2R by various
163 classes of ligands.

164

165 **Spectra of the antagonist- and inverse agonist-bound forms**

166 Next, we investigated the conformational changes induced by antagonists and inverse
167 agonists. Previous FTIR study showed that Atro-bound spectra clearly exhibited the different
168 spectral shift pattern of amide-I as compared to the ACh-bound spectra. The two positive bands
169 originating from Asn404^{6.52} and the tyrosine lid were absent, which might suggest a weaker
170 interaction of Atro with Asn404^{6.52} and a loose connecting triad of tyrosine lid³². With respect to
171 spectral features, Scopolamine (Scop)- and Ipratropium (Ipra)-bound spectra were similar with
172 Atro-bound spectra (Fig. 2b purple curves). Each antagonist-bound spectra possesses the

173 combination bands of amide-I at 1666 (-)/1655 (+)/1643 (-) cm^{-1} for Scop and 1664 (-)/1653
174 (+)/1643 (-) cm^{-1} for Ipra. As expected, the two ligand-binding site specific positive bands at
175 1687 and 1246 cm^{-1} are missing in both spectra, strongly indicating that all three antagonists
176 (Atro, Scop, and Ipra) bind to the orthosteric site of M_2R and induce a similar conformational
177 change in the TM region. These results are consistent with the structural similarity between these
178 antagonists. These antagonists differ only at cationic amine group, which forms an electrostatic
179 interaction with Asp103^{3,32,35}.

180 In contrast to antagonists, inverse agonists-bound spectra show significantly different
181 spectral features as compared to both antagonists- and agonists-bound spectra (Fig. 1b cyan
182 curves). For N-methylscopolamine (NMS)-bound spectra, dominant peaks at 1661 (+)/1643 (-)
183 cm^{-1} will correspond to amide-I band at 1656 (+)/1643 (-) cm^{-1} as observed in antagonists-bound
184 spectra. However, the corresponding negative 1666 cm^{-1} band is lacking in NMS-bound spectra.
185 Additionally, the band around 1660 cm^{-1} is broadened. For tiotropium (Tio)-bound spectra, in
186 addition to the amide-I pair bands at 1652 (+)/1640 (-) cm^{-1} , a new positive band was observed at
187 1666 cm^{-1} . The observed distinct spectral changes of amide-I band indicate conformational
188 heterogeneity in both NMS- and Tio-bound structures of M_2R . This is consistent with previous
189 NMR studies that revealed two conformations of M_2R upon binding with Tio²². Notably, both
190 inverse agonists-bound spectra showed no positive bands at 1687 and 1246 cm^{-1} originating from
191 Asn404^{6,52} and tyrosine lid, which is consistent with antagonists-bound spectra. Taken together,
192 different patterns of spectral shift of amide-I and spectral changes of functional group of amino
193 acids of the orthosteric binding site of M_2R were observed, depending on the efficacy of the
194 bound ligand.

195

196 **Correlation between relative intensities of the amide-I bands and the activation of**
197 **G protein**

198 To quantitatively examine the change in the amide-I band depending on the ligand efficacy,
199 the ratio of the band strength (1656 (+)/1666 (-) cm^{-1} in case of ACh-bound spectra, active state
200 component) at high frequency to the band strength at low frequency (1656 (+)/1640 (-) cm^{-1} in
201 case of ACh-bound spectra, inactive state component) was calculated by equation in Fig. 2a. The
202 amide-I percent population was assumed to be the ligand efficacy (Fig. 2b and 2c). Strikingly, all
203 agonists have an amide-I percent population >1 , with the exception of Xano. The amide-I percent
204 population for both the partial agonists and the antagonists were <1 . The ligands, Ixo (super
205 agonist) and NMS and Tio (inverse agonists) which gave a complex spectral variation, were
206 excluded from the present analysis. Compared to Pilo and McN among partial agonists, Xano
207 stabilizes a higher population of active-like M_2R conformation, which is characterized by the
208 outward movement of TM6. On the other hand, among the antagonists, Ipra has a higher ratio of
209 active conformation than Atro and Scop.

210 We assumed that the amide-I percent population correlates with M_2R signalling efficacy. To
211 quantitatively compare the two parameters, we calculated changes in the intensity of the amide-I
212 band by infrared spectroscopy and measured the efficacies of each ligand toward G_i -protein
213 activation using a NanoBiT G -protein dissociation assay (Extended Data Fig. 6)³⁶. The functional
214 assays show that three agonists; Meta, Are, and Carb which have similar chemical structures,
215 show almost identical G_i -protein activity as ACh-bound M_2R (Fig. 3a). Ixo represents higher
216 G -protein activation than ACh, which is consistent with the reported property of super agonist
217 (Fig. 3a)³⁴. We found that partial agonists, Pilo, McN, and Xano exhibit decreased G_i signalling
218 relative to ACh. By contrast, the tested antagonists showed poor (Ipra; 6.3% of ACh) or
219 undetectable (Atro and Scop) G_i -dissociation activity (Fig. 3a).

220 Next, we plotted the amide-I percent population for agonists, partial agonists, and antagonists
221 against their relative G_i -protein efficacy to ACh. The amide-I percent population correlated
222 remarkably well with agonist efficacy in promoting G_i coupling (E_{max}) (Fig. 3b), but did not

223 correlated with their potency values, pEC50 (Extended Data Fig. 7). In contrast, from the amide-I
224 percent population, the antagonists can induce an equilibrium shift to the active state at a certain
225 rate, but has a minimal or no apparent effect on G_i-protein activation (Fig. 3b, purple). These
226 results indicate that M₂R shows more conformational plasticity than other class A type of GPCRs
227 such as β₂AR¹⁸, turkey β₁AR¹⁹, μOR²⁰, and α_{1A}-AR²¹. Nevertheless, the band shift changes in
228 amide-I can be used as an infrared probe of agonist efficacy that promotes G_i-coupling.

229

230 **Implications of ligand-dependent dissociation kinetics from M₂R**

231 Additional insights on the discrimination of ligand efficacy from ATR-FTIR measurements
232 can be obtained by examining the ligand dissociation kinetics (k_{off}) from M₂R (Fig. 4a). In a
233 previous study, the time evolution of the difference ATR-FTIR spectra over the course of the
234 experiment showed different dissociation events between ACh and Atro with M₂R. While the
235 band intensity of amide-I in ACh-bound spectra decreased gradually after exchanging the buffer
236 without ACh, the band intensity in Atro-bound spectra did not decrease during the dissociation
237 phase artificially caused by the buffer exchange. These behaviours are consistent with their K_i
238 values (ACh; 10 μM³⁷, Atro; 0.8 nM^{38,39}). As shown in Fig. 4b, dissociation kinetics of Meta and
239 Carb was similar to ACh-bound M₂R. These results are consistent with similar ligand-bound
240 spectral features observed as shown in Fig. 1b. Although Are-bound M₂R also displayed similar
241 spectral features to that of ACh-bound spectra (Fig. 1b), its dissociation rate suggests slower
242 kinetics. This is probably due to the steric hindrance caused by the Are-specific chemical
243 structure possessing tetrahydropyridine, which makes it difficult to dissociate from the receptor.
244 On the other hand, Ixo exhibited the slowest dissociation kinetics. This result also indicates
245 difficulty in dissociating from the receptor and corresponds to previous NMR results suggesting
246 that Ixo binds more deeply in the ligand binding pocket than ACh²².

247 For partial agonists, while we observe fast dissociation kinetics of Pilo and McN like for ACh,

248 Xano exhibited extremely slow k_{off} . This can be likely explained by the tetrahydropyridine ring
249 present in the chemical structures of both Are and Xano⁴⁰. In addition, Xano is known to act as
250 the strongest G-protein biased agonist of M₂R⁴¹, and one of the underlying reasons for its strong
251 G-protein biased signalling could be a longer dissociation kinetics of the ligand-receptor complex.
252 With the exception of Are, Ixo, and Xano, all agonists and partial agonists we used in the present
253 study dissociated from M₂R by buffer exchange, whereas all antagonists and inverse agonists did
254 not show any dissociation from the receptor, which are consistent with their strong binding.
255 Given that the spectra of the inverse agonists-bound form are completely unique in shape
256 compared to other ligands-bound spectra, ligand binding-induced difference ATR-FTIR
257 spectroscopy appears to be a versatile tool to distinguish between antagonist and inverse agonist
258 binding to GPCRs.

259

260 **Discussion**

261 Here, taking advantage of ATR-FTIR spectroscopy, we investigated the conformational
262 changes of M₂R when bound to various ligands. The amide-I band shift pattern of α -helical C=O
263 stretch demonstrated that different classes of M₂R ligands altered the population between inactive
264 and active states, with the respect to the protein conformational changes, including an outward
265 movement of TM6. Furthermore, vibrational signals originating from functional group of key
266 amino acids (Asn404^{6,52} and tyrosine lid (Tyr104^{3,33}, Tyr403^{6,51}, and Tyr426^{7,39})) that constitute
267 the ligand binding pocket were varied by different ligand efficacy (Fig. 5).

268 In the previous NMR studies of ¹³C^εH₃-methionine-labeled β_2 AR¹⁸, turkey β_1 AR¹⁹, μ OR²⁰,
269 and α_{1A} -AR²¹, the chemical shifts reflecting receptor conformations for different ligands showed
270 a linear correlation with their ligand efficacies. On the other hand, a similar NMR analysis for
271 M₂R did not show a strong correlation with ligand efficacy, suggesting that M₂R showed a
272 complex conformational heterogeneity²². In the present study, by combining ATR-FTIR

273 spectroscopy with functional cell-based G_i -protein assays, we found a correlation between the
274 amide-I percent population and ligand efficacy for both full and partial agonists, but some ligands
275 such as Ixo or Xano showed complex spectral features and were outliers. Furthermore, all the
276 amide-I percent population of antagonists-bound spectra did not show linear correlation with
277 cell-based G_i -protein assay. Rather, the amide-I percent population analysis indicates that the
278 equilibrium proportions of active and inactive states of M_2R is similar between partial agonists
279 and antagonists. On the other hand, Asn404^{6,52} and tyrosine lid are likely involved in not only
280 direct ligand binding, but also allosteric activation of G-protein because the changes in Asn404^{6,52}
281 and Tyrosine lid are observed in the agonists- and partial agonists-bound spectra, but not in the
282 antagonists-bound spectra. These results demonstrate that M_2R shows more conformational
283 plasticity than other class A type of GPCRs such as β_2AR ¹⁸, turkey β_1AR ¹⁹, μOR ²⁰, and $\alpha_{1A}-AR$ ²¹,
284 and therefore future application of same ATR-FTIR measurements to these GPCRs may lead to a
285 confirmation.

286 Another noteworthy aspect of the present study is that the inverse agonists-bound spectra for
287 both NMS and Tio are significantly different from other ligands-bound spectra, especially in the
288 amide-I band region. The result of NMS-bound spectra showed a broadening of the amide-I band,
289 whereas the Tio-bound spectra was a bilobed amide-I band, indicative of unique conformational
290 changes as compared with other types of ligands. So, what are the inverse agonist-specific
291 structural changes compared to an antagonist, even though both ligands reduce the activation of
292 GPCRs? Recently determined structure of M_1R bound with Atro⁴² clearly showed significant
293 conformational differences as compared to Tio-bound M_1R ⁴³ at the extracellular end of TM5,
294 where a slight inward displacement at TM5 was observed in the Atro-bound form relative to Tio
295 binding. Most likely, the two arene ring of Tio causes steric clashes with TM5, which prevents the
296 inward movement of TM5 at the end of extracellular side like in Atro-bound M_1R . Thus, one of
297 the two positive bands of amide-I at 1666 cm^{-1} in the Tio-bound spectra may correspond to a

298 change in TM5 at extracellular region, while the other band at 1652cm^{-1} being specific to TM6
299 motion.

300 On the other hand, NMS does not have two arene rings like Tio, but rather a very similar
301 chemical structure to Scop (Fig. 1a). Nonetheless, how NMS can exhibit efficacy as an inverse
302 agonist? The only difference is the presence or absence of a methyl group in tropane alkaloid
303 between Scop and NMS. So, does the difference in efficacy depend solely on the presence or
304 absence of methyl groups between Scop (antagonist) and NMS (inverse agonist)? To investigate
305 this possibility, we measured ligand-binding induced difference ATR-FTIR spectroscopy of
306 Oxitropium (Oxitro) and N-butylscopolamine (NBS), possessing an ethyl or a butyl group in
307 tropane alkaloid, respectively. NBS-bound spectra was exactly identical to Scop-bound spectra,
308 while Oxitro-bound spectra exhibited a complex (broadening and/or bilobed) spectral feature like
309 in NMS-bound spectra, especially at the amide-I band (Fig. 6a). This result suggests that NBS
310 acts as an antagonist and Oxitro as an inverse agonist. The inactive structures of Atro-bound form
311 of M_1R ⁴² and NMS-bound form of M_2R ¹⁵ show a common involvement of Asp103^{3,32} in the
312 interaction with the tropane alkaloid (Fig. 6b). Thus, to function as an inverse agonist, the length
313 of the tropane alkaloid side chain should not be too long or too short, and only methyl or ethyl
314 groups adopts an energetically favourable conformation to connect tightly with Asp103^{3,32},
315 resulting in reducing the receptor activity (Extended Data Fig. 9).

316 Despite recent developments in structural biology methods, distinguishing the protein
317 conformational changes specific to the binding of an inverse agonist or antagonist remains
318 difficult. This is partly because the crystal structures of both inverse agonist- and
319 antagonist-bound forms show common structural changes, including an outward movement of
320 TM6 at the extracellular side and a corresponding inward shift of the intracellular end of TM6, as
321 seen in several structures of class A GPCR-ligand complexes⁴⁴. On the other hand, the ATR-FTIR
322 spectroscopic analysis performed in this study clearly distinguishes inverse agonists- and

323 antagonists-bound forms of M₂R by detecting the difference in the spectral feature of amide-I
324 band caused by the difference in carbon chain length, suggestive of its broad implications in
325 rational drug design of GPCRs (Extended Data Fig. 9).

326 Although we succeeded in distinguishing orthosteric ligand efficacy in M₂R, all of them that
327 we used in this study are water-soluble ligands. Our measurement system, which uses lipid
328 reconstituted samples, is incompatible with measurement for lipid-soluble ligands because of the
329 effect of protein shrinkage associated with lipid-ligand interaction. Therefore, future
330 improvements in measurement system is clearly needed to evaluate the efficacy of any ligand.
331 Moreover, since our method proved to be able to evaluate the efficacy of ligands for only one
332 type of receptor, it is necessary to demonstrate the general applicability of our method to a wide
333 range of other GPCRs in the future.

334 In summary, we have described a novel method for the quantitative evaluation of efficacy of
335 four types ligands including agonist, partial agonist, antagonist, and inverse agonist from the
336 vibrational perspective of amide-I band change in M₂R embedded into lipid environment using
337 ATR-FTIR spectroscopy. This biophysical technique can also provide the physicochemical
338 parameters such as dissociation constant and dissociation rate constant of ligand simultaneously.
339 Overall, the vibrational spectroscopic method reported herein provides a promising strategy for
340 measuring ligand efficacy at a wide variety of GPCRs.

341

342 **Methods**

343 **Protein expression and purification**

344 The M₂R fused with BRIL at ICL3 position (M₂R) was expressed and purified as described
345 previously¹⁵, except for some minor modifications for reconstitution into the membrane. Briefly,
346 C-terminally His-tagged M₂R-BRIL with the hemagglutinin (HA) signal sequence followed by an
347 N-terminal FLAG tag was expressed in Sf9 insect cells. Cells were infected at a density of 3–4 ×

348 10^6 cells/mL and grown for 48 h at 27 °C. Sf9 cells were lysed by osmotic shock in the presence
349 of 10 μ M atropine (Sigma-Aldrich). The lysed membranes were solubilized using a buffer
350 containing 30 mM HEPES-NaOH (pH 7.5), 0.75 M NaCl, 5 mM imidazole, 1 % (w/v)
351 n-dodecyl- β -D-maltopyranoside (DDM; anatrace), 0.2 % sodium cholate (Wako), 1 mg mL⁻¹
352 iodoacetamide (Dojindo), and Complete Protease inhibitor (Roche) for 1 h at 4 °C. The
353 supernatant was isolated by ultracentrifugation for 30 min at 140,000 \times g and incubated with
354 Ni-NTA Sepharose Superflow resin (Qiagen) overnight at 4 °C. After binding, the resin was
355 washed with Ni-NTA wash buffer: 30 mM HEPES-NaOH (pH 7.5), 0.75 M NaCl, 0.1 % (w/v)
356 DDM, 0.02 % (w/v) sodium cholate, 5 mM imidazole and 10 μ M atropine. The protein was then
357 eluted with Ni-NTA elution buffer: 30 mM HEPES-NaOH (pH 7.5), 0.75 M NaCl, 0.1 % (w/v)
358 DDM, 0.02 % (w/v) sodium cholate, 5 mM imidazole and 10 μ M atropine, 500 mM imidazole.
359 The eluate was supplemented with 2 mM calcium chloride and loaded onto an anti-FLAG M1
360 affinity resin (Sigma). The receptor was eluted from the anti-FLAG M1 affinity resin with a
361 buffer of 20 mM HEPES-NaOH (pH 7.5), 0.1 M NaCl, 0.01 % (w/v) DDM, 10 μ M atropine, 0.2
362 mg mL⁻¹ FLAG peptide and 5 mM EDTA. Finally, protein was purified by Superdex 200 Increase
363 size exclusion column (GE Healthcare) in a buffer of 20 mM HEPES-NaOH (pH 7.5), 0.1 M
364 NaCl, 0.01 % (w/v) DDM.

365

366 **Protein reconstitution**

367 For ATR-FTIR measurements, detergent-solubilized M₂R was reconstituted into asolectin
368 liposomes with a 20-fold molar excess. The detergent molecule was removed by incubation with
369 Bio-beads SM-2 (Bio-Rad, CA, USA). After removal of Biobeads, the lipid-reconstituted M₂R
370 was collected by ultracentrifugation for 30 min at 222,000 \times g at 4 °C. After several cycles of
371 wash/spin, lipid-reconstituted M₂R was suspended in a buffer composed of 5 mM phosphate (pH
372 7.5) and 10 mM KCl.

373

374 **Measurement of ligand binding-induced difference ATR-FTIR spectroscopy**

375 A 2 μL aliquot of the lipid-reconstituted M_2R suspensions was placed on the surface of a
376 silicon ATR crystal (three internal total reflection, Smith Detection, UK. After it was dried in a
377 gently natural drying, the sample was rehydrated with a solvent containing 200 mM phosphate
378 (pH 7.5) buffer with 140 mM NaCl, 3 mM MgCl_2 at a flow rate of 0.6 mL min^{-1} through a flow
379 cell, of which the temperature was maintained at $20 \text{ }^\circ\text{C}$ by circulating water. ATR-FTIR spectra
380 were first recorded at 2 cm^{-1} resolution, using an FTIR spectrometer (Bio-rad FTS7000, Agilent,
381 CA, USA) equipped with a liquid nitrogen-cooled MCT detector (an average of 768
382 interferograms). After the FTIR spectrum had been recorded in the second buffer with 1 mM
383 ligand, the difference FTIR spectrum was calculated by subtracting the data obtained for the first
384 and second buffer. The cycling procedure was repeated two to seven times, and the difference
385 spectra were calculated as the average of the presence minus absence spectra of ligand. The
386 spectral contributions of the unbound ligand, the protein/lipid shrinkage, and water/buffer
387 components were corrected (Extended Data Fig. 2-5).

388

389 **NanoBiT G-protein dissociation assay**

390 M_2R -induced G-protein dissociation was measured by a NanoBiT-G-protein dissociation assay³⁶,
391 in which the interaction between a $\text{G}\alpha$ subunit and a $\text{G}\beta\gamma$ subunit was monitored by the NanoBiT
392 system (Promega). Specifically, a NanoBiT- G_{i1} protein consisting of $\text{G}\alpha_{i1}$ subunit fused with a
393 large fragment (LgBiT) at the α -helical domain and an N-terminally small fragment
394 (SmBiT)-fused $\text{G}\gamma_2$ subunit with a C68S mutation was expressed along with untagged $\text{G}\beta_1$
395 subunit and M_2R . HEK293A cells were seeded in a 10-cm culture dish at a concentration of $2 \times$
396 $10^5 \text{ cells mL}^{-1}$ (10 mL per well in DMEM (Nissui) supplemented with 10 % fetal bovine serum
397 (Gibco), glutamine, penicillin and streptomycin), one day before transfection. Transfection

398 solution was prepared by combining 25 μL (per dish hereafter) of polyethylenimine (PEI) Max
399 solution (1 mg mL^{-1} ; Polysciences), 1 mL of Opti-MEM (Thermo Fisher Scientific) and a plasmid
400 mixture consisting of 1 μg M₂R (or an empty plasmid for mock transfection), 500 ng
401 LgBiT-containing G α_{i1} subunit, 2.5 μg G β_1 subunit and 2.5 μg SmBiT-fused G γ_2 subunit (C68S).
402 After an incubation for 1 day, the transfected cells were harvested with 0.5 mM EDTA-containing
403 Dulbecco's PBS, centrifuged and suspended in 10 mL of HBSS containing 0.01 % bovine serum
404 albumin (BSA; fatty acid-free grade; SERVA) and 5 mM HEPES (pH 7.4) (assay buffer). The
405 cell suspension was dispensed in a white 96-well plate at a volume of 80 μL per well and loaded
406 with 20 μL of 50 μM coelenterazine (Carbosynth) diluted in the assay buffer. After a 2 h
407 incubation at room temperature, the plate was measured for baseline luminescence (Spectramax L,
408 Molecular Devices) and a titrated test ligand (20 μL ; 6X of final concentrations) was manually
409 added. The plate was immediately read at room temperature for the following 5 min as a kinetics
410 mode, at measurement intervals of 20 sec. The luminescence counts over 3-5 min after ligand
411 addition were averaged and normalized to the initial count. The fold-change values were further
412 normalized to that of vehicle-treated samples and used to plot the G-protein dissociation response.
413 Using the Prism 8 software (GraphPad Prism), the G-protein dissociation signals were fitted to a
414 four-parameter sigmoidal concentration-response curve. For each replicate experiment, the
415 parameter *Span* (= *Top* – *Bottom*) of individual ligands was normalized to ACh and the resulting
416 E_{max} values were used as efficacy.

417

418 **Data Availability**

419 The data supporting the findings of this study are available in the article, Supplementary
420 Information, and if applicable, from the corresponding author on request.

421

422 **Reference**

- 423 1 Kenakin, T. Drug efficacy at G protein-coupled receptors. *Annu. Rev. Pharmacol. Toxicol.*
424 **42**, 349-379 (2002).
- 425 2 Weis, W. I.; Kobilka, B. K. The molecular basis of G protein-coupled receptor activation.
426 *Annu Rev Biochem.* **2018**, *87*, 897-919..
- 427 3 Manglik, A.; Kim, T. H.; Masureel, M.; Altenbach, C.; Yang, Z.; Hilger, D.; Lerch, M. T.;
428 Kobilka, T. S.; Thian, F. S.; Hubbell, W. L.; Prosser, R. S.; Kobilka, B. K. Structural
429 insights into the dynamics process of β_2 -adrenergic receptor signalling. *Cell* **2015**, *161*,
430 1101-1111.
- 431 4 Kobilka, B. K. & Deupi, X. Conformational complexity of G-protein-coupled receptors.
432 *Trends Pharmacol. Sci.* **28**, 397-406 (2007).
- 433 5 Rosenbaum, D. M., Rasmussen, S. G. & Kobilka, B. K. The structure and function of
434 G-protein-coupled receptors. *Nature* **459**, 356-363 (2009).
- 435 6 Wacker, D., Stevens, R. C. & Roth, B. L. How ligands illuminate GPCR molecular
436 pharmacology. *Cell* **170**, 414-427 (2017).
- 437 7 Kenakin, T. & Christopoulos, A. Analytical pharmacology: the impact of numbers on
438 pharmacology. *Trends Pharmacol. Sci.* **32**, 189-196 (2011).
- 439 8 Kenakin, T. Efficacy at G-protein-coupled receptors. *Nat. Rev. Drug. Discov.* **1**, 103-110
440 (2002).
- 441 9 Herenbrink, C. K., Sykes, D. A., Donthamsetti, P., Canals, M., Coudrat, T., Shonberg, J.,
442 Scammells, P. J. Capuano, B., Sexton, P. M., Charlton, S. J., Javitch, J. A., Christopoulos,
443 A. & Lane, J. R. The role of kinetic context in apparent biased agonism at GPCRs. *Nat.*
444 *Commun.* **7**, 10842-10856 (2016).
- 445
- 446 10 Katritch, V., Cherezov, V. & Stevens, R. C. Diversity and modularity of G protein-coupled
447 receptor structures. *Trends Pharmacol. Sci.* **33**, 17-27 (2012).
- 448 11 Warne, T., Edwards, P. C., Doré, A. S., Leslie, A. G. W. & Tate, C. G. Molecular basis for
449 high-affinity agonist binding in GPCRs. *Science* **364**, 775-778 (2019).
- 450 12 Liu, X., Xu, X., Hilger, D., Aschauer, P., Tiemann, J. K. S., Du, Y., Liu, H., Hirata, K.,
451 Sun, X., Guixà-González, R., Mathiesen, J. M., Hildebrand, P. W. & Kobilka, B. K.
452 Structural insights into the process of GPCR-G protein complex formation. *Cell.* **177**,
453 1243-1251 (2019).
- 454 13 García-Nafría, J. & Tate, C. G. Cryo-electron microscopy: Moving beyond X-ray crystal
455 structures for drug receptors and drug development. *Annu. Rev. Pharmacol. Toxicol.* **60**,
456 51-71 (2020).
- 457 14 Haga, K., Kruse, A. C., Asada, H., Yurugi-Kobayashi, T., Shiroishi, M., Zhang, C., Weis,
458 W. I., Okada, T., Kobilka, B. K., Haga, T. & Kobayashi, T. Structure of the human M2
459 muscarinic acetylcholine receptor bound to an antagonist. *Nature* **482**, 547-551 (2012).

- 460 15 Suno, R., Lee, S., Maeda, S., Yasuda, S., Yamashita, K., Hirata, K., Horita, S.,
461 Tawaramoto M. S., Tsujimoto, H., Murata, T., Kinoshita, M., Yamamoto, M., Kobilka, B.
462 K., Vaidehi, N., Iwata, S. & Kobayashi, T. Structural insights into the subtype-selective
463 antagonist binding to the M₂ muscarinic receptor. *Nat. Chem. Biol.* **14**, 1150-1158 (2018).
- 464 16 Kruse, A. C., Ring, A. M., Manglik, A., Hu, J.; Hu, K., Eitel, K., Hübner, H., Pardon, E.,
465 Valant, C., Sexton, P. M., Christopoulos, A., Felder, C. C., Gmeiner, P., Steyaert, J., Weis,
466 W. I., Garcia, K. C., Wess, J. & Kobilka, B. K. Activation and allosteric modulation of a
467 muscarinic acetylcholine receptor. *Nature* **504**, 101-106 (2013).
- 468 17 Maeda, S., Qu, Q., Robertson, M. J., Skinotis, G. & Kobilka, B. K. Structures of the M₁
469 and M₂ muscarinic acetylcholine receptor/G-protein complexes. *Science* **364**, 552-557
470 (2019).
- 471 18 Kofuku, Y., Ueda, T., Okude, J., Shiraishi, Y., Kondo, K., Maeda, M., Tsujishita, H. &
472 Shimada, I. Efficacy of the β_2 -adrenergic receptor is determined by conformational
473 equilibrium in the transmembrane region. *Nat. Commun.* **3**, 1045-1053 (2012).
- 474 19 Solt, A. S., Bostock, M. J., Shrestha, B., Kumar, P., Warner, T., Tate, C. G. & Nietlispach,
475 D. Insight into partial agonism by observing multiple equilibria for ligand-bound and
476 Gs-mimetic nanobody-bound β_1 -adrenergic receptor. *Nat. Commun.* **8**, 1795-1806 (2017).
- 477 20 Okude, J., Ueda, T., Kofuku, Y., Sato, M., Nobuyama, N., Kondo, K., Shiraishi, Y.,
478 Mizumura, T., Onishi, K., Natsume, M., Maeda, M., Tsujishita, H., Kuranaga, T., Inoue,
479 M. & Shimada, I. Identification of a conformational equilibrium that determines the
480 efficacy and functional selectivity of the μ -opioid receptor. *Angew. Chem. Int. Ed.* **54**,
481 15771-15776 (2015).
- 482 21 Wu, F-J., Williams, L. M., Abdul-Ridha, A., Gunatilaka, A., Vaid, T. M., Kocan, M.,
483 Whitehead, A. R., Griffin, M. D. W., Bathgate, R. A. D., Scott, D. J. & Gooley, P. R.
484 Probing the correlation between ligand efficacy and conformational diversity at the
485 α_{1A} -adrenoreceptor reveals allosteric coupling of its microswitches. *J. Biol. Chem.* **295**,
486 7404-7417 (2020).
- 487 22 Xu, J., Hu, Y., Kaindl, J., Risel, P., Hübner, H., Maeda, S., Niu, X., Li, H., Gmeiner, P., Jin,
488 C. & Kobilka, B. K. Conformational complexity and dynamics in a muscarinic receptor
489 revealed by NMR spectroscopy. *Molecular Cell* **75**, 1-15 (2019).
- 490 23 Wingler, L. M., Elgeti, M., Hilger, D., Latorraca, N. R., Lerch, M. T., Staus, D. P., Dror, R.
491 O., Kobilka, B. K., Hubbell, W. L. & Lefkowitz, R. J. Angiotensin analogs with divergent
492 bias stabilize distinct receptor conformations. *Cell* **176**, 468-478 (2019).
- 493 24 Kumar, S. & Barth, A. Following enzyme activity with infrared spectroscopy. *Sensors* **10**,
494 2626-2637 (2010).
- 495 25 Iwaki, M., Cotton, N. P. J., Quirk, P. G., Rich, P. R. & Baz Jackson, J. Molecular
496 recognition between protein and nicotinamide dinucleotide in intact, proton-translocating
497 transhydrogenase studied by ATR-FTIR spectroscopy. *J. Am. Chem. Soc.* **128**, 2621-2629

- 498 (2006).
- 499 26 Kitade, Y., Furutani, Y., Kamo, N. & Kandori, H. Proton release group of pharaonic
500 phoborhodopsin revealed by ATR-FTIR spectroscopy. *Biochemistry* **48**, 1595-1603
501 (2009).
- 502 27 Jiang, X., Zaitseva, E., Schmidt, M., Siebert, F., Engelhard, M., Schlesinger, R., Ataka, K.,
503 Vogel, R. & Heberle, J. Resolving voltage-dependent structural changes of a membrane
504 photoreceptor by surface-enhanced IR difference spectroscopy. *Proc. Natl. Acad. Sci. USA*
505 **105**, 12113-12117 (2008).
- 506 28 Doki, S., Kato, H. E., Solcan, N., Iwaki, M., Koyama, M., Hattori, M., Iwase, N.,
507 Tsukazaki, T., Sugita, Y., Kandori, H., Newstead, S., Ishitani, R. & Nureki, O. *Proc. Natl.*
508 *Acad. Sci. USA* **110**, 11343-11348 (2013).
- 509 29 Furutani, Y., Murata, T. & Kandori, H. Sodium or lithium ion-binding-induced structural
510 changes in the K-ring of V-ATPase from *Enterococcus hirae* revealed by ATR-FTIR
511 spectroscopy. *J. Am. Chem. Soc.* **133**, 2860-2863 (2011).
- 512 30 Katayama, K., Furutani, Y., Iwaki, M., Fukuda, T., Imai, H. & Kandori, H. “*In situ*”
513 observation of the role of chloride ion binding to monkey green sensitive visual pigment
514 by ATR-FTIR spectroscopy. *Phys. Chem. Chem. Phys.* **20**, 3381-3387 (2018).
- 515 31 Katayama, K., Nakamura, S., Sasaki, T., Imai, H. & Kandori, H. Role of Gln114 in
516 spectral tuning of a long-wavelength sensitive visual pigment. *Biochemistry* **58**,
517 2944-2952 (2019).
- 518 32 Katayama, K., Suzuki, K., Suno, R., Tsujimoto, H., Iwata, S., Kobayashi, T. & Kandori, H.
519 Ligand binding-induced structural changes in the M₂ muscarinic acetylcholine receptor
520 revealed by vibrational spectroscopy. *J. Phys. Chem. Lett.* **10**, 7270-7276 (2019).
- 521 33 Ballesteros, J. A. & Weinstein, H. Integrated methods for the construction of
522 three-dimensional models and computational probing of structure-function relationships
523 in G protein-coupled receptors. *Methods Neurosci.* 336-428 (1995).
- 524 34 Langmead, C. J. & Christopoulos, A. Supra-physiological efficacy at GPCRs: superstition
525 or super agonists? *Br. J. Pharmacol.* **169**, 353-356 (2013).
- 526 35 Heitz, F., Holzwarth, J. A., Gies, J. P., Pruss, R. M., Trumpp-Kallmeyer, S., Hibert, M. F.
527 & Guenet, C. Site-directed mutagenesis of the putative human muscarinic M₂ receptor
528 binding site. *Eur. J. Pharmacol.* **380**, 183-195 (1999).
- 529 36 Inoue, A., Raimondi, F., Kadji, F. M. N., Singh, G., Kishi, T., Uwamizu, A., Ono, Y.,
530 Shinjo, Y., Ishida, S., Arang, N., Kawakami, K., Gutkind, J. S., Aoki, J. & Russell, R. B.
531 Illuminating G-protein-coupling selectivity of GPCRs. *Cell* **177**, 1933-1947 (2019).
- 532 37 Cheng, K., Khurana, S., Chen, Y., Kennedy, R. H., Zimniak, P. & Raufman, J. P.
533 Lithocholylcholine, a bile acid/acetylcholine hybrid, is a muscarinic receptor antagonist. *J.*
534 *Pharmacol. Exp. Ther.* **303**, 29-35 (2002).
- 535 38 Kashihara, K., Varga, E. V., Waite, S. L., Roeske, W. R. & Yamamura, H. I. Cloning of the

536 rat m3, m4 and m5 muscarinic acetylcholine receptor genes by the Polymerase Chain
537 Reaction (PCR) and the pharmacological characterization of the expressed genes. *Life Sci.*
538 **51**, 955-971 (1992).

539 39 Kovacs, I., Yamamura, H. I., Waite, S. L., Varga, E. V. & Roeske, W. R. Pharmacological
540 comparison of the cloned human and rat M₂ muscarinic receptor genes expressed in the
541 murine fibroblast (B82) cell line. *J. Pharmacol. Exp. Ther.* **284**, 500-507 (1998).

542 40 Shannon, H. E., Bymaster, F. P., Calligaro, D. O., Greenwood, B., Mitch, C. H., Sawyer, B.
543 D., Ward, J. S., Wong, D. T., Olesen, P. H., Sheardown, M. J. et al. Xanomeline: a novel
544 muscarinic receptor agonist with functional selectivity for M₁ receptors. *J. Pharmacol.*
545 *Exp. Ther.* **269**, 271-281 (1994).

546 41 Jakubík, J., El-Fakahany, E. E. & Dolezal, V. Differences in kinetics of xanomeline
547 binding and selectivity of activation of G proteins at M₁ and M₂ muscarinic acetylcholine
548 receptors. *Mol. Pharmacol.* **70**, 656-666 (2006).

549 42 Maeda, S., Xu, J., Kadji, F. M. N., Clark, M. J., Zhao, J., Tsutsumi, N., Aoki, J., Sunahara,
550 R. K., Inoue, A., Garcia, K. C. & Kobilka, B. K. Structure and selectivity engineering of
551 the M₁ muscarinic receptor toxin complex. *Science*. **369**, 161-167 (2020).

552 43 Thal, D. M., Sun, B., Feng, D., Nawaratne, V., Leach, K., Felder, C. C., Bures, M. G.,
553 Evans, D. A., Weis, W. I., Bachhawat, P., Kobilka, T. S., Sexton, P. M., Kobilka, B. K. &
554 Christopoulos, A. Crystal structures of the M₁ and M₄ muscarinic acetylcholine receptors.
555 *Nature* **531**, 335-340 (2016).

556 44 Yin, W., Zhou, X. E., Yang, D., de Waal, P. W., Wang, M., Dai, A., Cai, X., Huang, C-Y.,
557 Liu, P., Wang, X., Yin, Y., Liu, B., Zhou, Y., Wang, J., Liu, H., Caffrey, M., Melcher, K.,
558 Xu, Y., Wang, M-W., Xu, H. E. & Jiang, Y. Crystal structure of the human 5-HT_{1B}
559 serotonin receptor bound to an inverse agonist. *Cell Discov.* **4**, 1-13 (2018).
560

561 **Acknowledgements**

562 We appreciate Drs. S. Gulati and M. Singh for helpful comments on the manuscript. We
563 thank Kayo Sato, Shigeko Nakano and Ayumi Inoue (Tohoku University) for their assistance with
564 plasmid preparation, maintenance of cell culture and cell-based GPCR assays. This work was
565 supported by JSPS KAKENHI, Japan, grant numbers 18K14662 to K.K., 18H03986, 19H04959
566 to H.K., 15K08268, 19H03428 to R.S., 19H05777 to S.I.; the Naito Science & Engineering
567 Foundation to K.K.; the Takahashi Industrial and Economic Research Foundation to K.K.; the
568 Takeda Science Foundation to T.K. and R.S.; the Naito Foundation to T.K.; the Koyanagi
569 Foundation to T.K.; the Basis for Supporting Innovative Drug Discovery and Life Science
570 Research (BINDS) from the Japan Agency for Medical Research and Development (AMED)
571 under grant number JP20am0101079 to S.I. and JP20am0101095 to A.I.; AMED under grant
572 number JP20gm0910007, JP20am0401020, and JP20ak0101103 to T.K. and the LEAP
573 JP20gm0010004 to A.I.; and Japan Science and Technology Agency (JST) PRESTO
574 (JPMJPR19G4) to K.K.

575

576

577 **Author Contributions**

578 K.K., K.S., R.S., A.I., and H.K. contributed to the study design. R.S. and H.T. expressed
579 samples in Sf9 and purified them. K.K. and K.S. reconstituted samples for spectroscopic
580 measurements. K.K. and K.S. conducted ATR-FTIR spectroscopic measurements. R.K. and A.I.
581 performed NanoBiT G-protein dissociation assay. K.K. prepared the initial manuscript and K.K.,

582 K.S., R.S., R.K., S.I., A.I., T.K. and H.K. wrote the paper with input from all the authors. All
583 authors discussed and commented on the manuscript.

584

585 **Additional information**

586 Supplementary Information accompanies this paper at <https://www.nature.com/ncomms/>

587

588 **Competing financial interests:** The authors declare no competing financial interests.

589 Reprints and permission information is available online at
590 <http://npg.nature.com/reprintsandpermissions/>

591

592 **Figures**

593

594 **Figure 1. Ligand binding-induced difference ATR-FTIR spectra measurement on**

595 **ligands with different efficacies for M₂R.** (a) Chemical structures of the ligands used in the

596 ATR-FTIR spectroscopy measurements. Common features among each ligand are marked by

597 dashed circles. (b) Ligand binding-induced difference ATR-FTIR spectra of M₂R bound with

598 various ligands at 293 K. Red, orange, purple, and cyan lines correspond to agonist-, partial

599 agonist-, antagonist-, and inverse agonist-bound spectra measured in H₂O, respectively. Positive

600 and negative bands originate from ligand-bound and ligand-unbound states, respectively. One

601 division of the y-axis corresponds to 0.002 absorbance unit.

602

603 **Figure 2. Ligand-dependent spectral changes in the α -helical region of M₂R and**

604 **relative populations of active and inactive states of M₂R.** (a) Ligand binding-induced

605 difference ATR-FTIR spectra in the 1800-1200 cm⁻¹ region, especially focusing on amide-I band

606 region, which are taken from Fig. 1B. Red and purple lines correspond to ACh- and Atro-bound

607 spectra, respectively. To quantitatively examine the change in the amide-I band specific to ligand
608 efficacy, the ratio between the band strength of (2)1656 (+)/(1)1666 (-) cm^{-1} of ACh-bound
609 spectra at high frequency and (2)1656 (+)/(3)1640 (-) cm^{-1} of ACh-bound spectra at low
610 frequency is calculated and reported as efficacy rate. (b) Ligand-dependent spectral changes of
611 amide-I band originating from C=O stretch of α -helix in 1700-1620 cm^{-1} region. Red, orange, and
612 purple lines correspond to agonist-, partial agonist-, and antagonist-bound spectra, respectively.
613 One division of the y-axis corresponds to 0.002 absorbance unit. (c) Relative populations of
614 active and inactive states upon ligand binding in M_2R derived by the equation of efficacy rate
615 from (A). The error values were calculated from three replicate experiments. Cyan dotted line
616 indicates the value = 1.

617

618 **Figure 3. Correlation between ligand efficacy and amide-I percent population.** (a)

619 Efficacies of the different M_2R ligands toward G_i activation in the NanoBiT G-protein
620 dissociation assay. E_{max} values were calculated from the concentration-response sigmoidal curves
621 in Extended Data Figure 6 and were normalized to that of ACh performed in parallel. Bars and
622 error bars represent mean and SEM, respectively, of 5 or 10 (shown in parenthesis) independent
623 experiments with each performed in duplicate. (b) Correlation between ligand efficacy and the
624 relative intensities of the amide-I bands. The relative intensities of the amide-I bands are
625 calculated by the equation of efficacy rate, which is derived from Figure 2c. Ligand efficacy is
626 determined by the NanoBiT G-protein dissociation assay from (a). Agonists (ACh, Meta, Are,
627 and Carb) are shown as red circles, partial agonists (Pilo, McN, and Xano) as orange circles, and
628 antagonists (Atro, Scop, and Ipra) as purple circles highlighted by light purple.

629

630 **Figure 4. Ligand-dependent dissociation kinetics on M_2R .** (a) Time trace of the

631 integrated absorbance signal in the amide-I band (red circle, ACh; purple circle, Atro) taken from

632 Ref 32. Ligand dissociation phase is highlighted by light blue. (b) Time trace of the integrated
633 absorbance signal at dissociation phase in the amide-I band for each ligand. Time-dependent
634 difference ATR-FTIR spectra upon ligand dissociation in the amide-I region ($1680\text{-}1630\text{ cm}^{-1}$) are
635 shown in Extended Data Fig. 8. Black red, orange, purple, and cyan correspond to ACh, agonist,
636 partial agonist, antagonist, and inverse agonist, respectively. Black dotted line represents the
637 fitting curve obtained by single exponential function.

638

639 **Figure 5. Proposed conformational changes in M₂R upon binding of ligands with**
640 **different efficacies.** (Upper) Schematic of M₂R TM6 and TM5 conformational states upon
641 binding of orthosteric ligands with different efficacies. TM6 features an open conformation in the
642 extracellular side and a closed conformation in the cytoplasmic side upon binding with inverse
643 agonist and antagonist. In contrast, TM6 features a closed conformation in the extracellular side
644 and an open conformation in the cytoplasmic side upon binding with both agonist and partial
645 agonist, which causes the opposite movement with both inverse agonist and antagonist. Yellow
646 dotted line indicates the orthosteric ligand binding pocket. (Lower) Schematic of M₂R ligand
647 binding pocket surrounded by TM3, 5, 6, and 7. Two key amino acids (Asn404^{6,52} and
648 Asp103^{3,32}) and tyrosine lid are depicted by star and oval markers, respectively. Binding of either
649 inverse agonist or antagonist opens the extracellular region of TM6, resulting in loosening of the
650 tyrosine lid, whereas both agonist- and partial agonist-bound forms compacts the ligand-binding
651 pocket, which induces the formation of tyrosine lid that excludes solvent entry.

652

653 **Figure 6. Comparison between the scopolamine derivatives.** (a) Chemical structures of
654 the scopolamine derivative ligands (Scopolamine (Scop), N-butylscopolamine (NBS),
655 Oxitropium (Oxipro), and N-methylscopolamine (NMS)) used in the current FTIR spectroscopic
656 studies, and each ligand bound spectra in the $1800\text{-}1450\text{ cm}^{-1}$ region. The group of quaternary

657 ammonium derivative positions are highlighted. Ligand binding-induced difference ATR-FTIR
658 spectra are measured in H₂O at 293 K. Positive and negative bands correspond to ligand-bound
659 and ligand-unbound states, respectively. One division of the y-axis corresponds to 0.0025
660 absorbance unit. (b) Comparison between Atro-bound structure in M₁R (green, PDB: 6WJC)⁴²
661 and NMS-bound structure in M₂R (cyan, PDB: 5YC8)¹⁵ at the view from extracellular side. The
662 amino acid residues and ligands are depicted by sticks, and TM helices are depicted by ribbons.
663 Hydrogen bond between Asp103^{3,32} and amine group of both ligands are shown by red dotted
664 lines with hydrogen bond length as labels.

665

666

667 **Extended Data Figures**

668

669 **Extended Data Fig. 1.** Comparison of IR absorption of each ligand. (a) Red and grey lines
670 represent agonist binding-induced difference ATR-FTIR spectra with empty liposome but without
671 protein and without both protein and empty liposome in the 1800-1150 cm⁻¹, respectively. One
672 division of the y-axis corresponds to 0.0003 absorbance unit. (b) Orange and grey lines represent
673 partial agonist binding-induced difference ATR-FTIR spectra with empty liposome but without
674 protein and without both protein and empty liposome in the 1800-1150 cm⁻¹, respectively. One
675 division of the y-axis corresponds to 0.001 absorbance unit. (c) Purple and grey lines represent
676 antagonist binding-induced difference ATR-FTIR spectra with empty liposome but without
677 protein and without both protein and empty liposome in the 1800-1150 cm⁻¹, respectively. One
678 division of the y-axis corresponds to 0.0005 absorbance unit. (d) Cyan and grey lines represent
679 agonist binding-induced difference ATR-FTIR spectra with empty liposome but without protein
680 and without both protein and empty liposome in the 1800-1150 cm⁻¹, respectively. One division
681 of the y-axis corresponds to 0.0015 absorbance unit.

682

683

684 **Extended Data Fig. 2.** The agonist binding-induced difference ATR-FTIR spectra in the
685 4000-1000 cm^{-1} region. The absorption of unbound ligands (shaded grey), the absorption of
686 phosphate buffer (shaded green), the absorption of water (shaded cyan) and the absorption of CO_2
687 (shaded yellow) are subtracted for spectral correction.

688

689 **Extended Data Fig. 3.** The partial agonist binding-induced difference ATR-FTIR spectra in the
690 4000-1000 cm^{-1} region. The absorption of unbound ligands (shaded grey), the absorption of
691 phosphate buffer (shaded green), the absorption of water (shaded cyan) and the absorption of CO_2
692 (shaded yellow) are subtracted for spectral correction.

693

694 **Extended Data Fig. 4.** The antagonist binding-induced difference ATR-FTIR spectra in the
695 4000-1000 cm^{-1} region. The absorption of unbound ligands (shaded grey), the absorption of
696 phosphate buffer (shaded green), the absorption of water (shaded cyan) and the absorption of CO_2
697 (shaded yellow) are subtracted for spectral correction.

698

699 **Extended Data Fig. 5.** The inverse agonist binding-induced difference ATR-FTIR spectra in
700 the 4000-1000 cm^{-1} region. The absorption of unbound ligands (shaded grey), the absorption of
701 phosphate buffer (shaded green), the absorption of water (shaded cyan) and the absorption of CO_2
702 (shaded yellow) are subtracted for spectral correction.

703

704 **Extended Data Fig. 6.** Concentration-response curves of G_i activation in NanoBiT G-protein
705 dissociation assay of M_2R . Symbols and error bars represent mean and SEM, respectively, of 5 or
706 10 (shown in parenthesis) independent experiments with each performed in duplicate.

707

708 **Extended Data Fig. 7.** (a) Potency of the different M₂R ligands toward G_i activation in the
709 NanoBiT G-protein dissociation assay. pEC₅₀ values were calculated from the
710 concentration-response sigmoidal curves in Extended Data Figure 6. Bars and error bars represent
711 mean and SEM, respectively, of 5 or 10 (shown in parenthesis) independent experiments with
712 each performed in duplicate. (b) Plot of the amide-I percent population for agonists, partial
713 agonists, and antagonists against their potency toward G_i activation in the NanoBiT G-protein
714 dissociation assay. The amide-I percent population values were calculated by the equation of
715 efficacy rate, which was derived from Figure 2c, and pEC₅₀ values were derived from (a).
716 Agonists (ACh, Meta, Are, and Carb) were shown as red circles, partial agonists (Pilo, McN, and
717 Xano) as orange circles, and antagonists (Atro, Scop, and Ipra) as purple circles.

718

719 **Extended Data Fig. 8.** Time-dependent difference ATR-FTIR spectra upon agonist (1st panel),
720 partial agonist (2nd panel), antagonist (3rd panel) and inverse agonist (4th panel) dissociating in
721 the amide-I (at 1680-1630 cm⁻¹) region.

722

723 **Extended Data Fig. 9.** Schematic drawing of binding fashion between antagonist and inverse
724 agonist. Pale purple squares indicate the different moiety in tropane alkaloid among each ligand;
725 Scopolamine (Scop), N-butylscopolamine (NBS), Oxitropium (Oxitro), and
726 N-methylscopolamine (NMS). Pale cyan squares indicate the common chemical moiety among
727 each ligand. Only NMS can fit the length between TM3 and TM6, which adopts an energetically
728 favourable binding fashion to M₂R resulting in reducing the receptor activity at negative value.

Figures

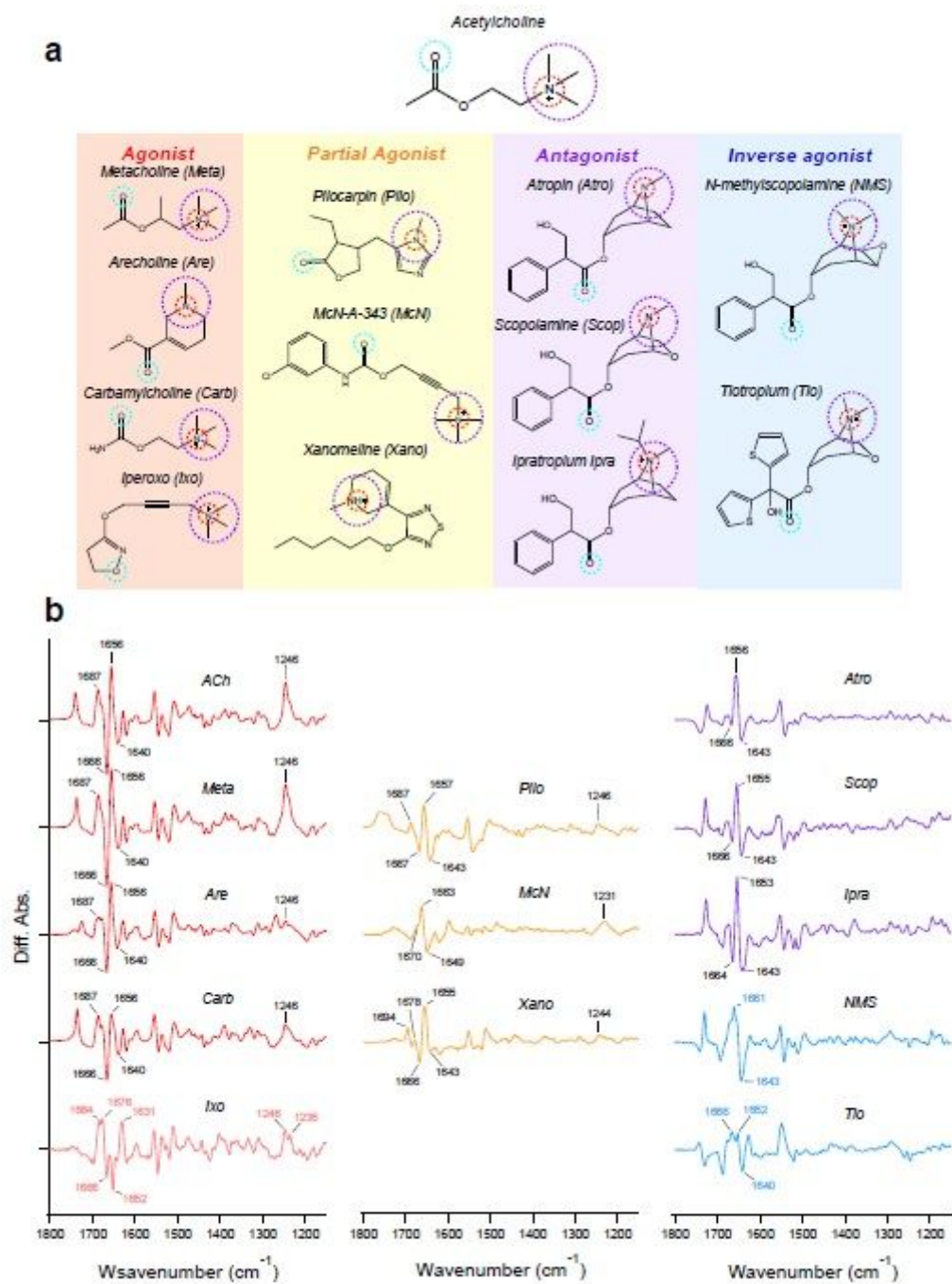


Figure 1

Ligand binding-induced difference ATR-FTIR spectra measurement on ligands with different efficacies for M2R. (a) Chemical structures of the ligands used in the ATR-FTIR spectroscopy measurements. Common features among each ligand are marked by dashed circles. (b) Ligand binding-induced difference ATR-FTIR spectra of M2R bound with various ligands at 293 K. Red, orange, purple, and cyan lines correspond to agonist-, partial agonist-, antagonist-, and inverse agonist-bound spectra measured in H₂O,

respectively. Positive and negative bands originate from ligand-bound and ligand-unbound states, respectively. One division of the y-axis corresponds to 0.002 absorbance unit.

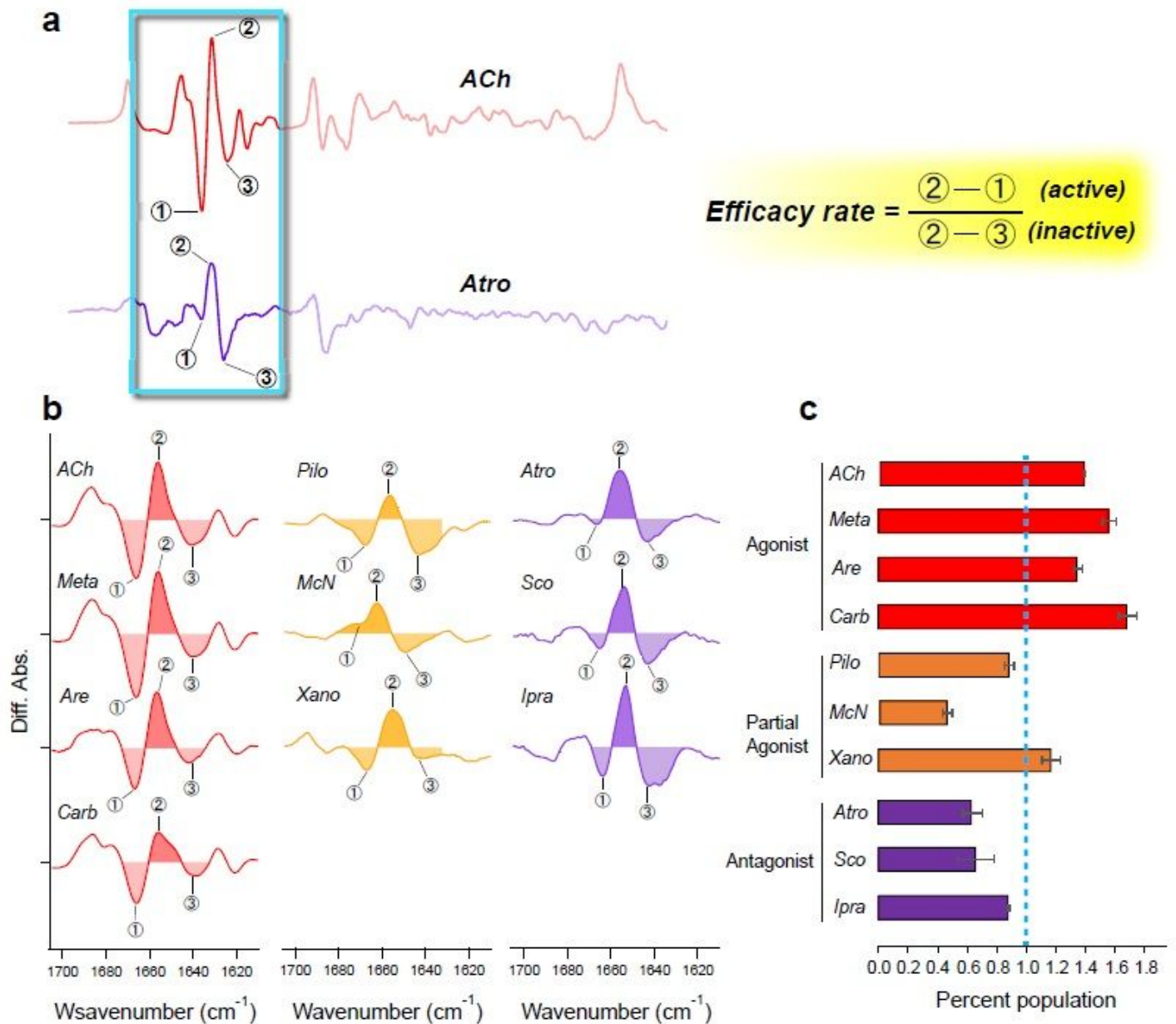


Figure 2

Ligand-dependent spectral changes in the α -helical region of M2R and relative populations of active and inactive states of M2R. (a) Ligand binding-induced difference ATR-FTIR spectra in the 1800-1200 cm⁻¹ region, especially focusing on amide-I band region, which are taken from Fig. 1B. Red and purple lines correspond to ACh- and Atro-bound spectra, respectively. To quantitatively examine the change in the amide-I band specific to ligand efficacy, the ratio between the band strength of (2)1656 (+)/(1)1666 (-) cm⁻¹ of ACh-bound spectra at high frequency and (2)1656 (+)/(3)1640 (-) cm⁻¹ of ACh-bound spectra at low frequency is calculated and reported as efficacy rate. (b) Ligand-dependent spectral changes of amide-I band originating from C=O stretch of α -helix in 1700-1620cm⁻¹ region. Red, orange, and purple

lines correspond to agonist-, partial agonist-, and antagonist-bound spectra, respectively. One division of the y-axis corresponds to 0.002 absorbance unit. (c) Relative populations of active and inactive states upon ligand binding in M2R derived by the equation of efficacy rate from (A). The error values were calculated from three replicate experiments. Cyan dotted line indicates the value = 1.

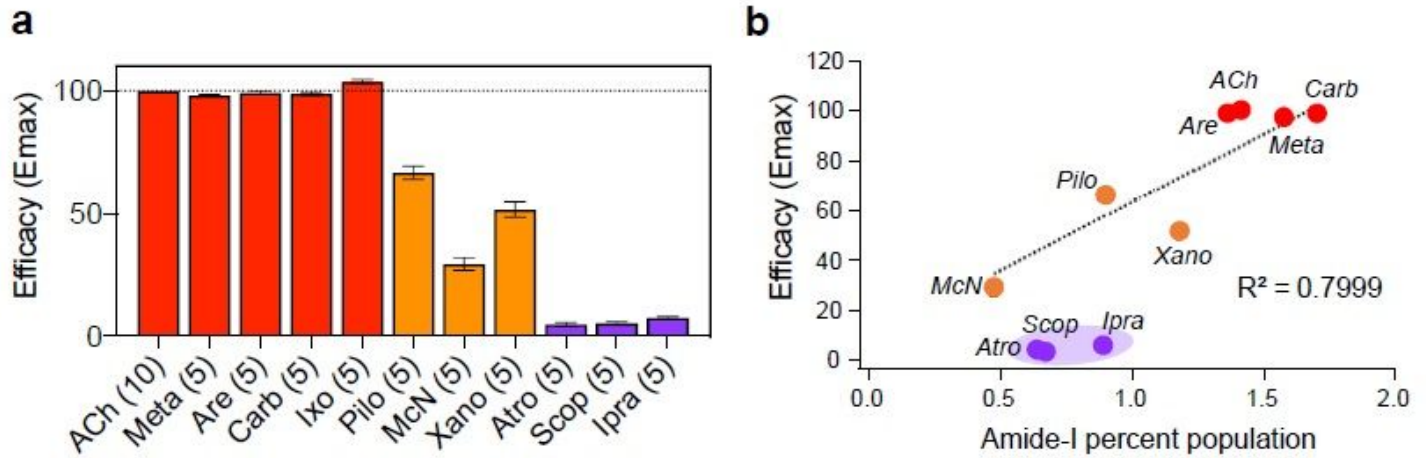


Figure 3

Correlation between ligand efficacy and amide-I percent population. (a) Efficacies of the different M2R ligands toward Gi activation in the NanoBiT G-protein dissociation assay. Emax values were calculated from the concentration-response sigmoidal curves in Extended Data Figure 6 and were normalized to that of ACh performed in parallel. Bars and error bars represent mean and SEM, respectively, of 5 or 10 (shown in parenthesis) independent experiments with each performed in duplicate. (b) Correlation between ligand efficacy and the relative intensities of the amide-I bands. The relative intensities of the amide-I bands are calculated by the equation of efficacy rate, which is derived from Figure 2c. Ligand efficacy is determined by the NanoBiT G-protein dissociation assay from (a). Agonists (ACh, Meta, Are, and Carb) are shown as red circles, partial agonists (Pilo, McN, and Xano) as orange circles, and antagonists (Atro, Scop, and Ipra) as purple circles highlighted by light purple.

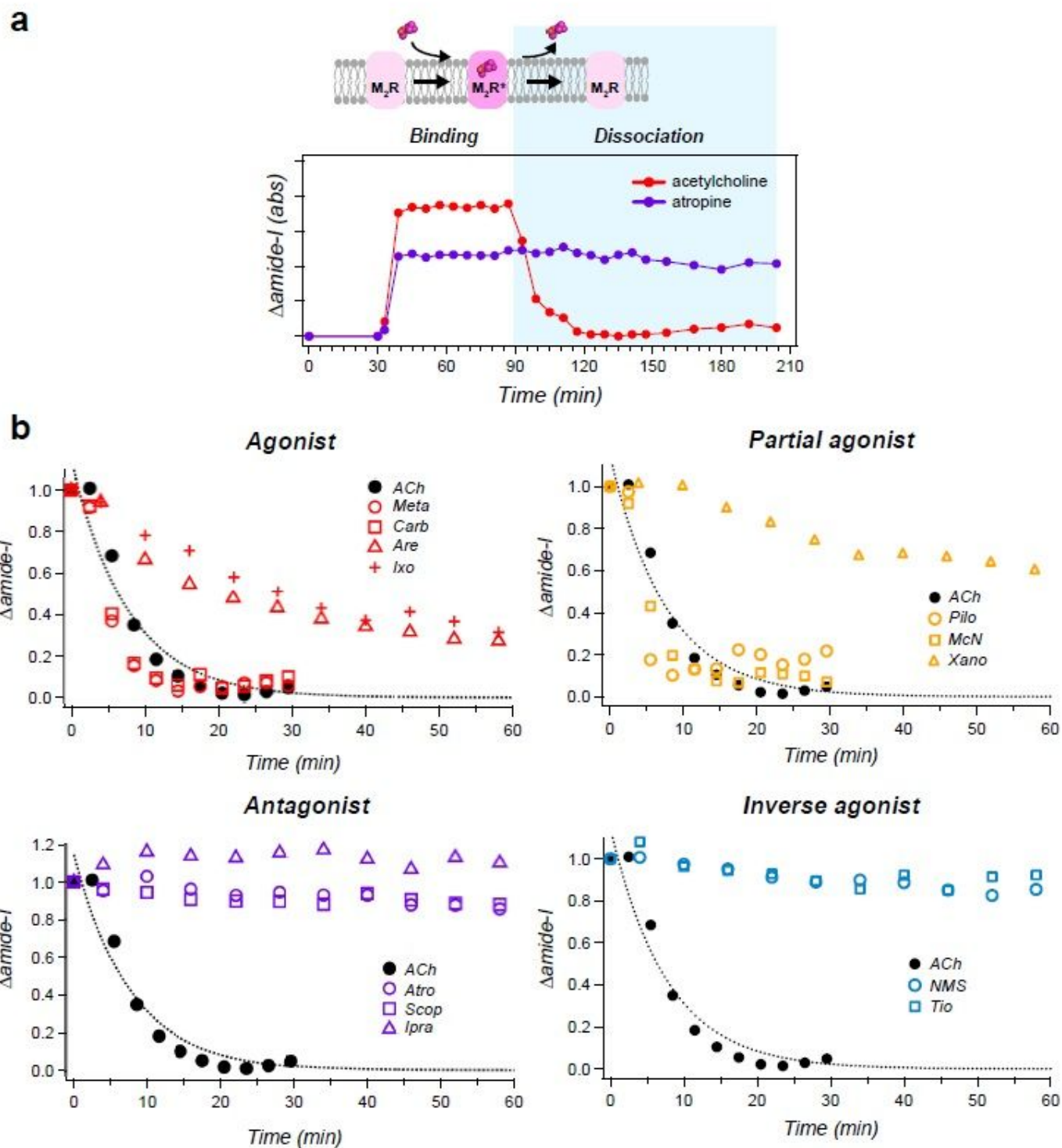


Figure 4

Ligand-dependent dissociation kinetics on M2R. (a) Time trace of the integrated absorbance signal in the amide-I band (red circle, ACh; purple circle, Atro) taken from Ref 32. Ligand dissociation phase is highlighted by light blue. (b) Time trace of the integrated absorbance signal at dissociation phase in the amide-I band for each ligand. Time-dependent difference ATR-FTIR spectra upon ligand dissociation in the amide-I region (1680-1630 cm^{-1}) are shown in Extended Data Fig. 8. Black red, orange, purple, and

cyan correspond to ACh, agonist, partial agonist, antagonist, and inverse agonist, respectively. Black dotted line represents the fitting curve obtained by single exponential function.

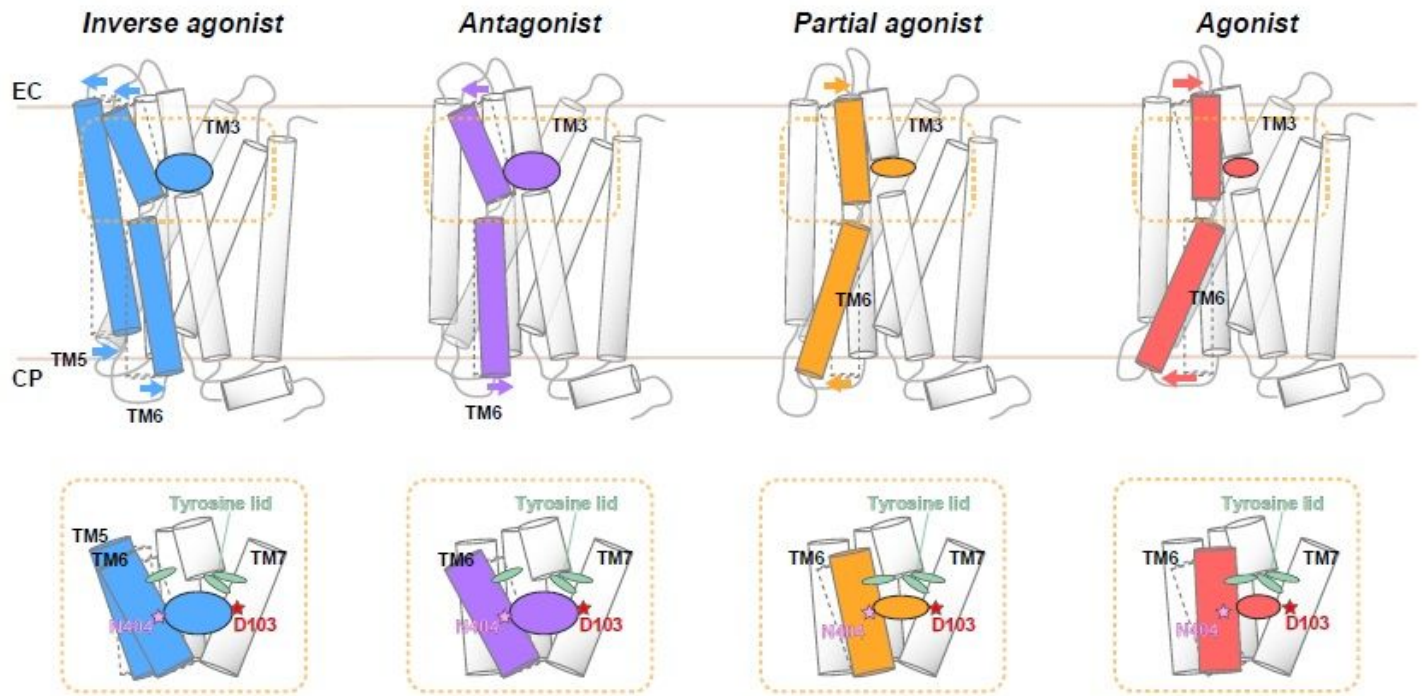


Figure 5

Proposed conformational changes in M2R upon binding of ligands with different efficacies. (Upper) Schematic of M2R TM6 and TM5 conformational states upon binding of orthosteric ligands with different efficacies. TM6 features an open conformation in the extracellular side and a closed conformation in the cytoplasmic side upon binding with inverse agonist and antagonist. In contrast, TM6 features a closed conformation in the extracellular side and an open conformation in the cytoplasmic side upon binding with both agonist and partial agonist, which causes the opposite movement with both inverse agonist and antagonist. Yellow dotted line indicates the orthosteric ligand binding pocket. (Lower) Schematic of M2R ligand binding pocket surrounded by TM3, 5, 6, and 7. Two key amino acids (Asn404.52 and Asp1033.32) and tyrosine lid are depicted by star and oval markers, respectively. Binding of either inverse agonist or antagonist opens the extracellular region of TM6, resulting in loosening of the tyrosine lid, whereas both agonist- and partial agonist-bound forms compacts the ligand-binding pocket, which induces the formation of tyrosine lid that excludes solvent entry.

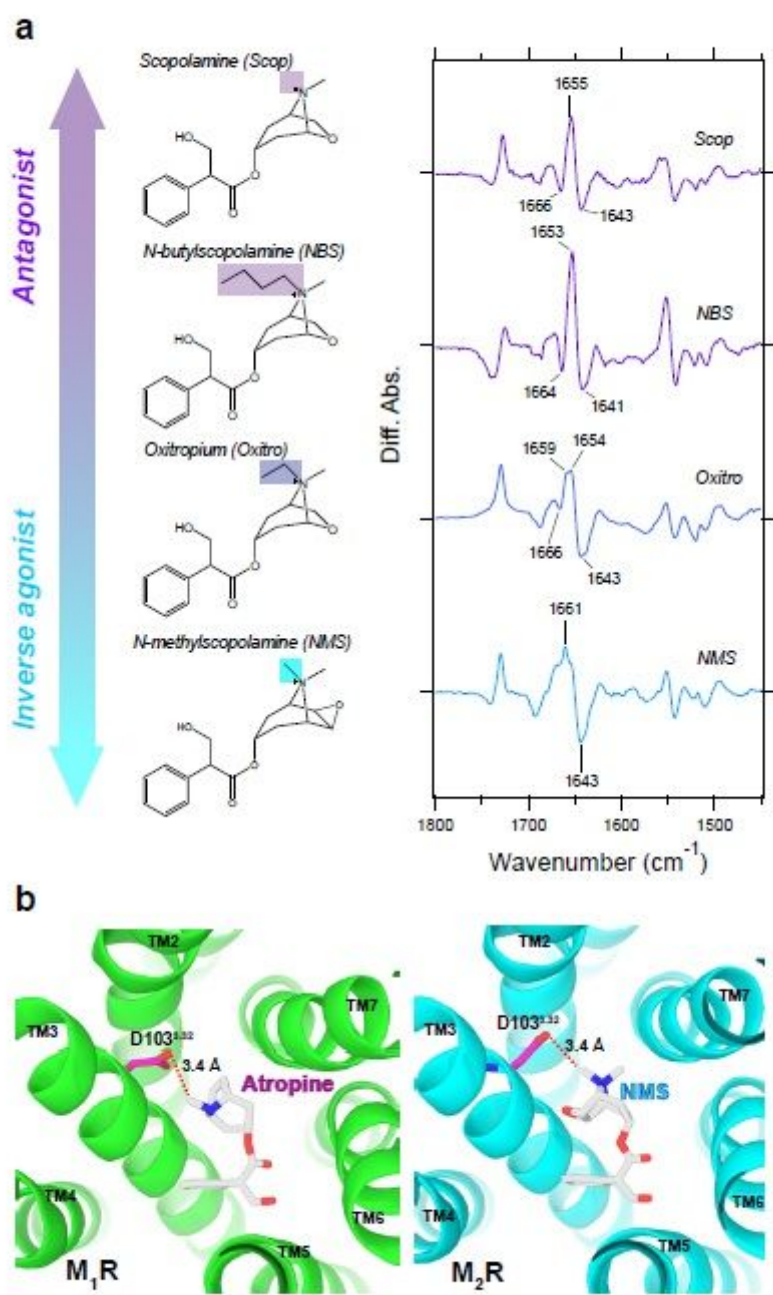


Figure 6

Comparison between the scopolamine derivatives. (a) Chemical structures of the scopolamine derivative ligands (Scopolamine (Scop), N-butylscopolamine (NBS), Oxitropium (Oxipro), and N-methylscopolamine (NMS)) used in the current FTIR spectroscopic studies, and each ligand bound spectra in the 1800-1450 cm^{-1} region. The group of quaternary ammonium derivative positions are highlighted. Ligand binding-induced difference ATR-FTIR spectra are measured in H_2O at 293 K. Positive and negative bands correspond to ligand-bound and ligand-unbound states, respectively. One division of the y-axis corresponds to 0.0025 absorbance unit. (b) Comparison between Atro-bound structure in M_1R (green, PDB: 6WJC)42 and NMS-bound structure in M_2R (cyan, PDB: 5YC8)15 at the view from extracellular side.

The amino acid residues and ligands are depicted by sticks, and TM helices are depicted by ribbons. Hydrogen bond between Asp1033.32 and amine group of both ligands are shown by red dotted lines with hydrogen bond length as labels.

Supplementary Files

This is a list of supplementary files associated with this preprint. Click to download.

- [M2ligandscreeningSupportingFiguresv2.pdf](#)